

Layer Shape LiFePO₄ Obtained by Powder Extrusion Molding as Solid Boosters for Ferro/Ferricyanide Catholyte in Semisolid Redox Flow Battery: Effect of Porosity and Shape

Jose F. Vivo-Vilches,^{*[a]} Álvaro Vázquez-Navalmoral,^[a] Carmen de la Torre-Gamarra,^[a] Jesús Cebollada,^[b] Alejandro Várez,^[a] and Belén Levenfeld^[a]

Powder extrusion molding is proposed to fabricate ceramic LiFePO₄ layers (0.5–1.0 mm thickness) as solid booster for ferricyanide electrolyte in semisolid redox flow battery. In some extruded layers, the binder is partially decomposed, while in others it is completely removed and, afterwards, the material is sintered, so materials with different porosity and dimensions are obtained. After characterizing the materials, the kinetics for the reaction with ferricyanide is evaluated, being the binderless materials the ones which react faster and reach larger

degrees of oxidation. For the material with 1.0 mm thick comparable results to the ones already published are obtained (69% capacity for LiFePO₄ compared to the theoretical value). In the case of the 0.5 mm thick sintered solid, an outstanding performance is achieved, reaching almost the theoretical capacity (94%) with a very high coulombic efficiency (> 99%) at 1 mA cm⁻², results that were only obtained at much lower current densities in previous works.

Introduction

The climatic emergency and the increasing energy demand are hastening the implementation of renewable energy sources all over the world.^[1–4] Nevertheless, there are still many challenges to solve, that make it impossible to meet all the demand with an energy mix based only on renewable energy.^[5–7] While research effort has been made to overcome some of these obstacles related to the materials such as durability, cost, recyclability or efficiency, there is an unavoidable limitation in this kind of systems, which is their intrinsic intermittency.^[7–9] Since they depend on weather and atmospheric phenomena, it is not possible to match the production to the demand. Because of that, efficient energy storage devices are needed to overcome this issue, being the most common the electrochemical ones.^[9,10]

Redox flow batteries (RFBs) represent nowadays one of the most promising energy storage devices for this type of

stationary applications.^[11,12] An RFB is a battery in which the electrochemical energy is stored in the electrolyte, while the electrochemical cell is only responsible for the electron transfer from the grid to the solution at the electrode surface. Thus, the solution has to be pumped from the tanks, where it is stored, to the cell, which has two compartments separated by an ion-exchange membrane. This configuration has a series of advantages regarding its implementation in the electrical grid such as: power and energy decoupling; not losing the stored energy in case of power surge or any other problem affecting the electrochemical cell (since the energy is stored in the electrolytes that are stored in the tanks, so the flow can be stopped); the electrochemical cells can be relatively small, since the amount of energy will be controlled by the volume of the tanks and the concentrations of the solutions.^[11,13,14]

The most studied and developed technology for RFBs is the one based on vanadium species, since this element can be present in several oxidation states, so the same electrolyte can be employed in both half-cells.^[15–17] Nevertheless, the rising and unstable price of this element,^[18] besides the fact that very acidic and corrosive electrolytes need to be employed, potentiated the research on alternative compounds for RFBs such as aqueous-organic electrolytes (AORFBs) and coordination compounds.^[19,20] Among these lasts, ferro/ferricyanide redox couple [Fe(CN)₆]^{3/4-} is presented as a sound alternative for the catholyte, due to its fast electron transfer kinetics, almost full reversibility, low price and the fact that it can work in neutral electrolytes.^[21] For this compound, its main drawback is its low solubility compared to the one of the compounds that commonly act as anolyte (such as sulfonated anthraquinones).^[22]

[a] Dr. J. F. Vivo-Vilches, Á. Vázquez-Navalmoral, Dr. C. de la Torre-Gamarra, Prof. A. Várez, Prof. B. Levenfeld
Departamento de Ciencia e Ingeniería de Materiales e Ingeniería Química
Universidad Carlos III de Madrid
Avda. Universidad 30, 28911, Leganés, Spain
E-mail: jvivo@ing.uc3m.es

[b] Dr. J. Cebollada
Instituto de Catálisis y Petroleoquímica
Consejo Superior de Investigaciones Científica (CSIC)
Calle Marie Curie 2, 28049, Madrid, Spain

 Supporting information for this article is available on the WWW under <https://doi.org/10.1002/batt.202200050>

 © 2022 The Authors. *Batteries & Supercaps* published by Wiley-VCH GmbH. This is an open access article under the terms of the Creative Commons Attribution License, which permits use, distribution and reproduction in any medium, provided the original work is properly cited.

An approach to increase the capacity of RFBs is the so-called redox targeting, firstly reported in 2013 by Huang et al.^[23] In this semisolid RFB setup, a material that can react with the liquid electrolyte is introduced in the tank and acts as a solid booster. The solid is immobilized inside the tank, while the soluble molecule (the so-called mediator) is mainly used to transport the charge between the electrode and the solid booster.^[24,25] In this pioneer work, Huang et al.^[23] employed two mediators, one for the oxidation of the solid (with a higher reduction potential) and the other for the reduction (with a lower one). Conceptually, this is the simplest way to proceed, but it comes at a price: the difference between charge and discharge voltages substantially increases, thus, lowering the voltage efficiency.^[26–28] Furthermore, the complexity of solutions implies that side reactions between different forms of the two mediators might appear, producing irreversible capacity loss due to the formation of precipitates or unactive species.^[29] The same group reported in 2016 the first RFB containing LFP (LiFePO_4) as solid booster with a single mediator.^[30] In this case, the mediator was the iodine/iodide(I_2/I_3^-) redox couple that, according to Nernst equation, showed a higher or lower reduction potential than the one of the solid, depending on the relative concentration of the two species. Both works developed non-aqueous RFB containing electrolytes dissolved in organic solvents commonly used in lithium-ion batteries (TEGDME and carbonates). Later, in 2018, this research group reported the first example of a complete RFB containing solid boosters in both tanks and in aqueous media: [$\text{LiTi}_2(\text{PO}_4)_3$ -LTP-inside the negative tank with sulfides as mediators and LiFePO_4 -LFP- with ferricyanide in the positive].^[31] A mixed solvent strategy was proposed which consisted of adding TEGDME to water to adjust the potential of the mediators to the one of the solids. After these pioneer works, several authors have proposed different materials to be used as solid boosters for ferricyanide including LFP,^[26,32] Prussian blue,^[33] copper hexacyanoferrate,^[28] or nickel hydroxide.^[22] From these investigations a clear conclusion can be obtained; as the solid booster is immobilized inside the tank and the electrochemical cell does not have information about its state of charge (SOC), the charge-discharge curves depend on the SOC of the solution.^[22,26] Therefore, cutoff voltages can be rapidly reached before the solid is completely charged or discharged. Because of it, controlling the kinetics of the reaction between the solid and the mediator in solution is crucial to maximize the boosting capacity of the material.^[26,34,35]

Reaction kinetics can be improved by modifying different factors such as temperature or concentration; but in the case of heterogeneous reactions there is another crucial factor to consider that is the diffusion of the reactants through the solid matrix.^[26] In order to favor it, controlling the morphology of the solid in terms of porosity, shape and size becomes essential, so the proportion of solid area that can react with the species in solution can be increased. Several synthetic routes and molding techniques have been proposed in the case of LFP, especially with the research effort to fabricate ultrathick ceramic (additive-free) electrodes for maximizing the capacity of Li-ion and Na-ion batteries.^[36–40] Among them, powder extrusion

molding (PEM) presents several advantages for industrial applications such as: being a continuous process, rapidness, easiness, low cost and easy scalability.^[37,41] Furthermore, the shape and the thickness of the extruded materials can be controlled by the die located at the exit of the extruder, allowing to obtain for instance films, cylindrical filaments or prismatic ones. This technique was proposed in previous works of our group for the fabrication of thick ceramic LFP^[37] and LTO^[38] (lithium titanium oxide) electrodes for Li-ion batteries with enhanced areal capacities ($12\text{--}15 \text{ mAh cm}^{-2}$). Both electrodes, LTO and LFP, were successfully tested in a full battery obtaining an outstanding volumetric energy density of 340 mWh cm^{-3} after 100 charge/discharge cycles.^[38]

In this work, extruded LFP layers fabricated by PEM are used as solid boosters for ferrocyanide catholyte in semisolid RFB. Intermediate samples are separated along the process to better understand the changes produced in the materials along the different treatments. After characterizing the physicochemical properties of extruded samples by different techniques (thermogravimetric analysis, mercury intrusion porosimetry, scanning electron microscopy, X-ray diffraction) and the kinetic of the reaction with the oxidized form of the mediator, selected samples are tested as solid boosters of ferrocyanide in a symmetric RFB containing an excess of the soluble specie in the anolyte. This setup allows us to prove the superior behavior of these materials compared to the ones published up to date for this system.

Results and Discussion

Sample preparation and characterization

Extruded samples were prepared following the procedure detailed elsewhere.^[37] Briefly, LFP powder was mixed with a binder containing polypropylene (PP) as structural polymer, paraffin wax (PW) for controlling the viscosity and stearic acid (SA) as surfactant in a proportion previously optimized (55.0% LFP, 22.5% PP, 20.7% W, 1.8% SA, by volume). After homogenization in the mixer, the obtained feedstock was extruded using two different nozzles with rectangular shape (6.0 mm width, 0.5 or 1.0 mm height) allowing to obtain 6.0 mm wide layer shape samples with two different thickness (0.5 and 1.0 mm). The temperature profile along the extrusion barrel was optimized in the temperature range between 175 and 185 °C. Once extruded, the pieces were treated to eliminate the binders following the procedure depicted in Figure S1: in a first solvent debinding step, extruded materials were immersed in n-heptane at 50 °C for 1 h to remove the PW and SA (Figure S1a); then PP was eliminated by thermal debinding at 350 °C for 30 min or 45 min under nitrogen to partially decompose the polymer (Figure S1b) or at 450 °C for 1 h to ensure its complete elimination (Figure S1c); for these lasts, a final sintering step (750 °C, 1 h, N_2) was performed to improve their poor mechanical stability of the materials (Figure S1d). In the case of 0.5 mm thickness samples, intermediate samples were obtained after solvent debinding (LFPsd) and partial

decomposition of PP (LFP30 and LFP45), while for both thicknesses (0.5 and 1.0 mm) sintered samples were produced (LFP0.5sint and LFP1.0sint).

After processing, for samples with same thickness but different PP content and porosity, PP proportion left in samples (%PP_{TGA}) was quantified by thermogravimetric analysis (TGA) through the weight loss occurring starting at 300 °C in nitrogen atmosphere (Figure S2). Porosity was characterized by means of mercury intrusion porosimetry to obtain the open porosity (% Pores), the volume of pores accessible to mercury (V_{Hg}) and the mean pore width (d_p). These data are shown in Table 1. This

last technique was also employed to obtain the pore size distribution (PSD) curves depicted in Figure 1.

As expected, since PP is not solubilized by the n-heptane, it remained the same after the solvent debinding step, only increasing its relative proportion since the PW and the SA were eliminated. After the treatments at 350 °C, around a third of the total PP was removed after 30 min (LFP30, 6.7%wt), while almost half of it was eliminated when treated for 45 min (LFP45, 5.0%wt). This partial decomposition produces an increase in porosity (pore volume) and an enlargement of the pore sizes. PSD curves also show a homogenization in the pore width (sharper peaks) with the subsequent treatments. In such a way, the porosity resulted very heterogeneous in the case of LFPsd, with pores of almost every size up to 200 nm. This heterogeneity completely disappeared even for the first thermal treatment. This fact reveals two things: this heterogeneous porosity formed by the pores with smaller diameter is coming from the interparticle void within PP particles formed after the removal SA and PW; as PP is a thermoplastic polymer, it melts before decomposing (at 160 °C), and this melting provokes the loss of this PP structure. After the complete decomposition of PP and sintering, a further increase in the macropore volume is observed.

In order to analyze the samples surface, scanning electron microscopy (SEM) images were obtained (Figure S3). Using backscattered electron (BSE) detector, two phases can be easily differentiated, corresponding to LFP (brighter) and PP (darker), confirmed by energy dispersive spectroscopy (EDS) mapping (Figure 2). Micrographs of the LFPsd (Figure S3a) and LFP45 (Figure S3b) samples revealed the presence of PP stacks along the materials, being the size of these stacks smaller after partial thermal decomposition. For the LFP0.5sint (Figure S3c) only LFP is observed. EDS mappings for carbon (Figure 2b), iron (Figure 2c) and phosphorus (Figure 2d) were obtained at the surface of LFP45, confirming that these stacks are formed by PP, since a larger proportion of C was identified in this region, compared to the Fe and P rich phase conforming the rest of the samples.

As crystalline structures of LFP and iron phosphate (FePO₄, FP) are slightly different, X-Ray diffraction (XRD) is a very useful

Table 1. Samples properties obtained by TGA and Hg porosimetry.

Sample	%PP _{TGA} [%wt]	%Pores [%v]	V_{Hg} [cm ³ g ⁻¹]	d_p [nm]
LFPsd	8.8	27.3	0.136	67.7
LFP30	6.7	29.2	0.152	176.7
LFP45	5.0	34.6	0.177	178.9
LFP0.5sint	0.0	38.9	0.198	194.4
LFP1.0sint	0.0	38.4	0.190	201.8

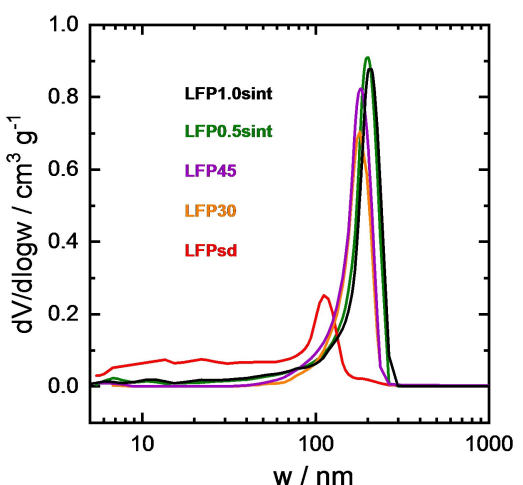


Figure 1. Pore size distribution curves for the samples LFPsd, LFP30, LFP45 and LFP0.5sint.

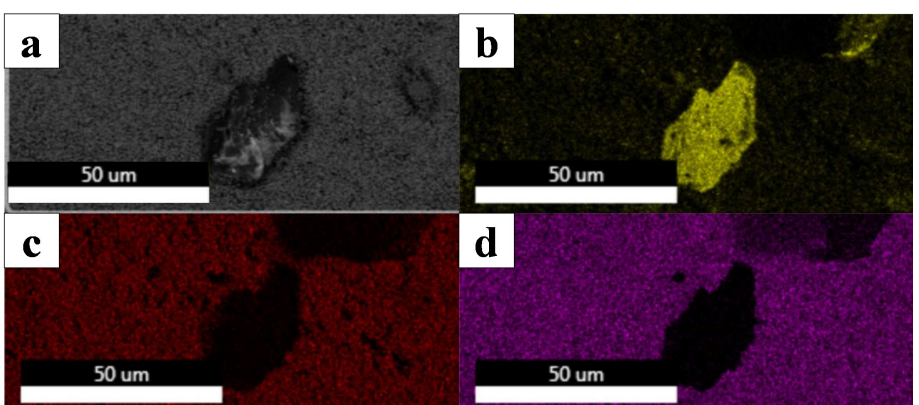


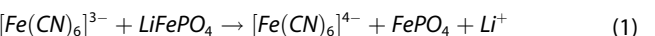
Figure 2. a) SEM image and b-d) EDS mapping of a PP stack from sample LFP45, b) carbon, c) iron, d) phosphorus.

technique to detect the delithiation of the sample surface.^[26] XRD patterns for the samples (Figure 3) displayed only the main peaks of LFP, indicating the absence of the oxidized sample (FP). The presence of PP is very difficult to detect by this technique due to the very relative amount and the low crystallinity as compared with LFP.

LiFePO₄ and Fe(CN)₆³⁻ reaction kinetics

As mentioned above, kinetics of the oxidation reaction plays a key role to achieve a good performance in this kind of batteries. Since the solid is immobilized, and the solution is the only part of the electrolyte entering into the electrochemical cell, a fast diffusion of the liquid through the solid is critical to maximize the solid contribution to the capacity. For this reason, kinetics studies were used as a screening test to select which of

the samples could be used in the battery. The reaction between the oxidized form of the mediator and the LFP is depicted in Equation (1).



Concentration variation of Fe(CN)₆³⁻ versus time can be followed by UV-VIS. From it, the amount of oxidized material along time can be calculated by stoichiometry, and the extent of the reaction was limited by the solid since the oxidized mediator was in excess regarding the solid material (5:2 in moles). Since in all the cases the reaction is the same and the raw material is C-coated LFP, differences in kinetics that are observed should be related to diffusional limitations, thus, related to differences in accessibility of the solution to the entire porosity of solids.

Firstly, kinetic experiments for sintered samples (LFP0.5sint and LFP1.0sint) were performed (Figure 4), to evaluate the influence of the thickness. Variation on concentration of the Fe(CN)₆³⁻ (Figure 4a) and oxidized LFP (%LFP_{ox}) (Figure 4b) for both materials revealed the importance of the thickness in the reaction rate. As expected, the smaller the thickness, the faster was the reaction and, also the larger became the final proportion of oxidized LFP.

Diffusion of the solution through the porosity of the material is necessary for the reaction to occur, so a reduction in the thickness of the material will be critical to improve it, considering that both samples present very similar porosity. Thus, LFP0.5sint presented a faster kinetics, being oxidized up to 55% after 12 h of reaction (versus 44% for LFP1.0sint). This difference was accentuated at larger times, being the values of %LFP_{ox} after 24 h 75% for LFP0.5sint and 55% for LFP1.0sint. Moreover, while the plot for LFP1.0sint showed an asymptotic behavior, meaning that the reaction was about to reach the equilibrium, in the case of LFP0.5sint, %LFP_{ox} was further increased up to 80% after 30 h and it seems it could reach larger values.

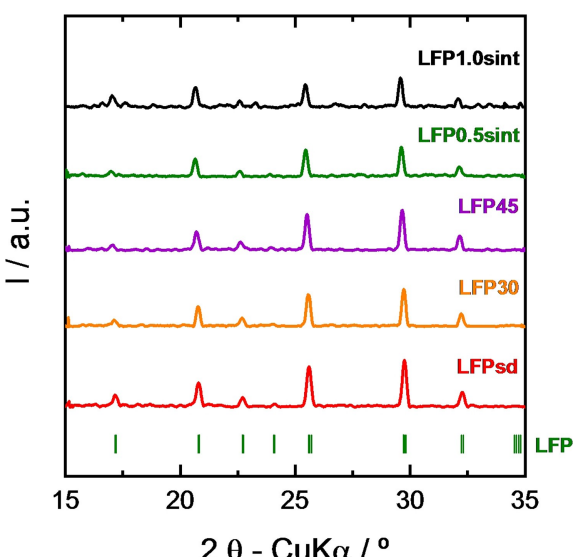


Figure 3. X-Ray diffraction patterns of the sample surface LFPsd, LFP30, LFP45, LFP0.5sint and LFP1.0sint.

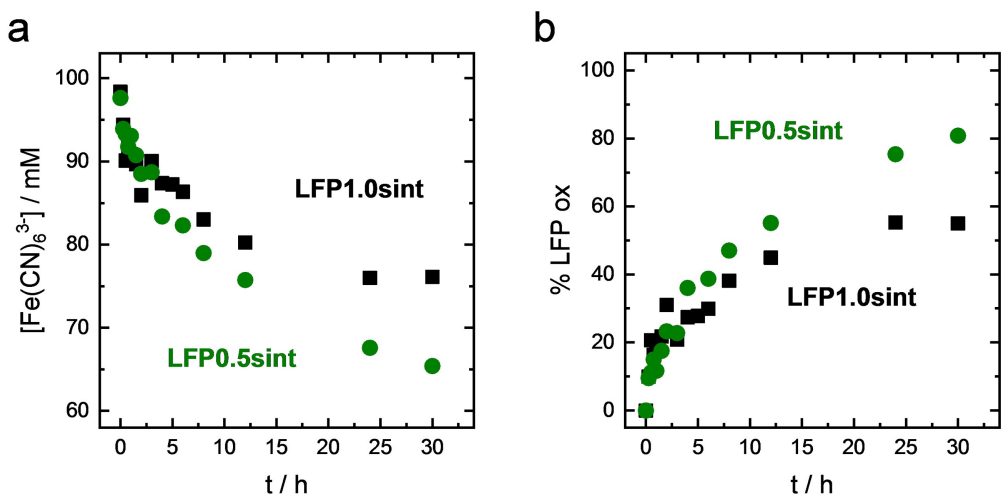


Figure 4. Kinetics of the oxidation reaction of Fe(CN)₆³⁻ with LFP0.5sint (●) and LFP1.0sint (■). a) Variation of [Fe(CN)₆³⁻] and b) %LFP_{ox} with t.

After evaluating the influence of the thickness, reaction kinetics for the samples LFPsd and LFP45 were obtained and compared to the one for LFP0.5sint (Figure 5a) to study the influence of porosity. LFPsd sample presented a slower reaction kinetics than LFP0.5sint, achieving a %LFP_{ox} of 41% after 12 h and 52% after 24 h. Considering that the diffusion rate is related to the solid accessible surface, it was expected that the sample LFP45 with an intermediate porosity would perform worse than LFP0.5sint but better than LFPsd; however, the reaction kinetics for the oxidation of LFP45 resulted extremely poor, being oxidized only up to a 20% after 24 h.

Trying to explain this extremely low value for the sample LFP45, XRD patterns were performed on the surface of the samples (pellet) before and after the oxidation. Also, one pellet of LFP45 was grinded and the resulting powder was analyzed by XRD. As it can be seen in Figure 5(b), the XRD patterns for all the samples surface only present the main peaks of the FePO₄, while for the grinded powder, the LiFePO₄ diffraction signals also appear. From the intensity of the main peak for each phase, it is deduced that lithiated phase is majority. This difference between the composition of LFP45 surface and the bulk after oxidation indicates that redox chemical reaction, and the corresponding Li extraction, only takes place at outermost surface, indicating that the oxidizing solution is unable to penetrate through the porosity of this sample. The most reasonable explanation for this is that remaining PP was hindering the diffusion of the solution through the material porosity. Given these poor results, samples containing PP were not selected for subsequent tests in the battery.

Results for the kinetics pointed out the importance of tailoring the shape, porosity and dimensions of the materials to increase the reaction rate and to favor the material utilization (enlarging as much as possible the surface in contact with the liquid electrolyte). With a smaller thickness, LFP0.5sint presents a larger surface to volume ratio than LFP1.0sint, and, in such a way, the active area in contact with the solution was substantially increased, favoring the oxidation of a larger

proportion of the material. Because of the same reason, for samples extruded with the same thickness, porosity and accessibility resulted crucial.

Galvanostatic charge-discharge (GCD) of the redox flow battery (RFB)

Selected materials were tested as solid booster for ferro/ferricyanide electrolyte. To analyze their electrochemical performances, galvanostatic charge-discharge (GCD) experiments were performed in a symmetric RFB in which the anolyte and the catholyte were at the same concentration (0.1 M) but the volume was different for both, being larger in the case of the anolyte (50 mL) than in the case of the catholyte (15 mL). In such a way, the half-cell limiting the capacity was the positive one (0.015 mol, 40.2 mAh), so the increase in capacity produced after adding LFP as a solid booster could be analyzed. Details about electrolyte preparation and electrochemical setup were included in the experimental section. As done in a previous work from Vivo-Vilches et al.,^[26] a mixed solvent strategy was employed to equalize the electrochemical potential of the solution with the one of the solid, so oxidation and reduction reactions can be controlled by the relative concentration of oxidizing and reducing forms of the mediator (Nernst Equation).

GCD curves for different experimental conditions are depicted in Figure 6. To start the experiments, the battery was in a fully discharged state (state of charge, SOC=0). Then, a GCD curve was obtained for the liquid electrolytes at 1 mA cm⁻², ensuring that it reached its theoretical capacity (40.2 mAh) and that the charge-discharge process was fully reversible (coulombic efficiency close to 100%). Then, 250 mg of LFP0.5sint or LFP1.0sint (theoretical increase of the capacity, +42.6 mAh, since LFP has a theoretical capacity of 170.5 mAh g⁻¹) were added to the system and GCD curves were obtained at 1 mA cm⁻² (Figure 6a).

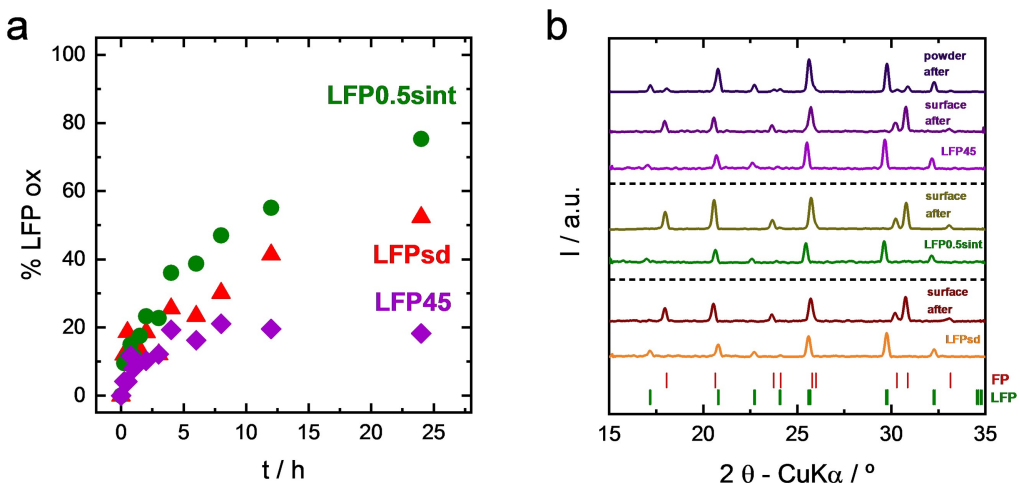


Figure 5. a) Variation of %LFP_{ox} with t for the samples LFPsd, LFP45 and LFP0.5sint. b) X-Ray diffraction patterns of the surface of each sample before and after the reaction. For the LFP45 sample, the whole pellets were grinded, and powders were analyzed by XRD.

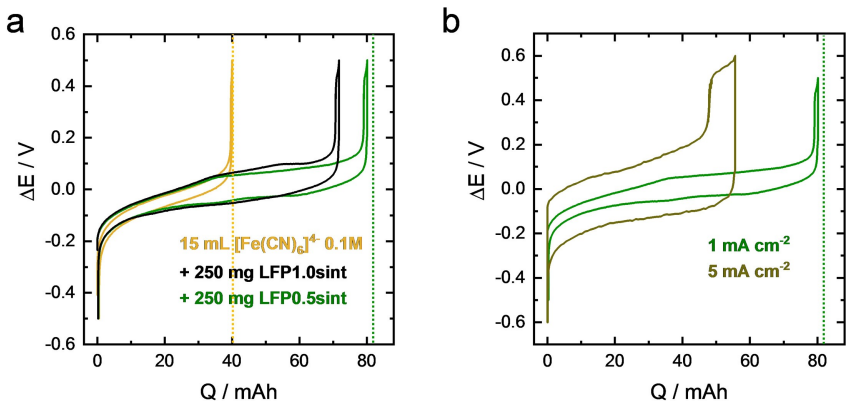


Figure 6. GCD curves. a) At 1 mA cm^{-2} for $0.1 \text{ M } \text{Fe}(\text{CN})_6^{4-}$, after adding 250 mg of LFP1.0sint and after adding 250 mg LFP0.5sint. b) Results for LFP0.5sint at different current densities.

The catholyte containing LFP0.5sint reached a capacity of 80.1 mAh, so the increase due to the addition of the booster resulted 39.9 mAh, corresponding to a utilization of 93.6% of the solid (calculated by comparing the experimental value with the theoretical one). Furthermore, a very high coulombic efficiency was achieved ($> 99\%$), so the capacity fading would be minimum in the case of this electrolyte. In contrast, and in good agreement with kinetic results, the increase in capacity obtained when thicker LFP1.0sint pieces were added to the catholyte resulted much lower (71.8 mAh of total capacity, with an increase of +29.2 mAh, 68.5% of LFP), while the coulombic efficiency resulted still very high.

As demonstrated before for the kinetics studies, these results confirmed the importance of controlling the thickness of the extruded solids when employed as solid boosters, maximizing the surface to volume ratio to favor diffusion. This allows to increase the area of solid in contact with the solution, leading to larger utilization of it, so the capacity of the electrolyte can be further increased when adding LFP0.5sint. For this material, GCD experiment was also performed at a larger current density 5 mA cm^{-2} (Figure 6b); for an RFB, as the current density increases, the voltage efficiency decreases, what it is clearly observed in our results (the difference between charge and discharge voltages is more pronounced for the curve obtained at 5 mA cm^{-2}). As expected, increasing the current density also worsened the utilization of the solid, being the %LFP of 23.0% compared to the 93.6% achieved when the battery was charged at 1 mA cm^{-2} ; this was foreseeable considering that this increase produced a reduction in the liquid electrolyte charge time from around 40 h to 8 h, thus, the contact time was significantly reduced. In this case, the extra plateau observed at around 0.5 V was not considered for the calculation of charge capacity, since it is not sure that it corresponds to LFP oxidation. In the case of the experiment performed at 1 mA cm^{-2} the %LFP resulted much higher than in the case of the kinetics for the same time; this apparent contradiction can be easily explained attending to the difference between the two experimental setups. While in the case of the battery setup the cell is continuously oxidizing the mediator and the SOC is continuously increasing, in the kinetics

experiments the relative concentration of the oxidizing form of the mediator is constantly reduced, down to values lower than 70%. According to the previous work from Vivo-Vilches et al.^[26] who analyzed the influence of ferro/ferricyanide relative concentrations in the degree of oxidation achieved, at this concentration the mediator is not able to completely oxidize the material (Figure 5 of this published work). This difference between kinetic results and battery performance should be less pronounced at shorter times, when the decrease in concentration is not so marked, while deviations may be observed at longer times. This is exactly what we observed in our results when comparing both experiments for the same material.

With the aim of comparing the performance of our materials, results for other materials proposed for the same system found in literature are shown (Table 2). In this table, data about the experimental procedure (material processing; theoretical charge capacity, Q_t ; current density, j) and results (experimental charge capacity, Q_{exp} ; degree of utilization for the solid during charge, %Solid_{ch}; coulombic efficiency, Q.Ef.) are included. It can be observed that, until this work, values of %LFP over 90% with more than $> 99\%$ Q.Ef. were only obtained at very low current densities (0.25 mA cm^{-2}), thus, taking a very long time for charging and discharging the battery. Moreover, our results for LFPsint0.5 obtained at a larger current density 5 mA cm^{-2} are in the order of those obtained by other authors at 1 mA cm^{-2} . Finally, results for LFPsint1.0 are also better than most of the published results, demonstrating that PEM is a very

Table 2. Samples properties obtained by TGA and Hg porosimetry.

Sample	Processing	Q_t [mAh]	Q_{exp} [mAh]	%Sol _{ch} [%]	j $[\text{mA cm}^{-2}]$	Q.Ef. [%]
LFP1.0sint	PEM	83	72	69	1.00	> 99
LFP0.5sint	PEM	83	50	23	5.00	> 99
LFP0.5sint	PEM	83	80	94	1.00	> 99
LFP40 ^[26]	SPS	660	473	45	1.00	96
LFP40 ^[26]	SPS	660	656	99	0.25	> 99
LFPpell ^[31]	Pelletized	238	138	38	1.25	> 99
Pr. Blue ^[33]	Granulated	318	246	55	20.00	> 99
Ni(OH) ₂ ^[22]	NiMH com.	754	364	40	2.00	> 99

effective technique to process sintered ceramic materials that will be employed as RFB solid boosters.

Conclusion

The main challenge for the use of semisolid setups in RFB is maximizing the capacity/amount of solid ratio; in other words, the actual apport of the solid to the capacity should be as close as possible to the theoretical value. The solid can be added to the electrolyte in the form of granules that will flow, but this setup comes with an increase in flow resistance which makes hard to implement them at an industrial scale. This was the main reason that made researchers to focus in redox-mediated type system, being the solid immobilized in the tank. The bottlenecks for the development of this kind of RFB are two: finding suitable couples of active materials and soluble active species; reaction kinetics between the solid and the mediator.

While finding new material/mediator couples is a very challenging and interesting research field, it needs to be kept in mind that ferro/ferricyanide system is an ideal electrolyte for RFB, being its main drawback its low capacity. For increasing this capacity, as demonstrated in this work, the second bottleneck has to be addressed, starting by a rational design of the material, testing processing techniques not employed for this kind of systems up to date and analyzing the results for optimizing the properties of the materials.

Our data revealed the importance of having solid with well-developed porosity and an optimal thickness to increase the surface to volume ratio of the materials. Thanks to this rational material design and processing, outstanding performances were achieved. In the case of LFP0.5sint, almost over 90% of the theoretical capacity for the solid (94%) was obtained with $>99\%$ columbic efficiency at 1 mA cm^{-2} . These results are much better than the ones published till now for this kind of system, where the experimental increase in capacity was always below 50% with respect to the theoretical one at this current density.

Experimental Section

Reagents

C-coated LiFePO₄ (Linyi Gelon Lib Co., LTD); polypropylene Isplen PP090G2M (Repsol-YPF); paraffin wax (99%, Panreac); stearic acid (99%, Panreac); potassium ferrocyanide ($\text{K}_4\text{Fe}(\text{CN})_6 \cdot 3\text{H}_2\text{O}$, Sigma-Aldrich); potassium ferricyanide ($\text{K}_3\text{Fe}(\text{CN})_6$, Sigma-Aldrich); lithium chloride (LiCl, Sigma-Aldrich); dimethyl sulfoxide (DMSO, Sigma-Aldrich).

Instruments

For the sample preparation, a Haake Rheocord 252p mixer and a Haake Rheomex OS single screw extruder were employed. Thermogravimetric analysis (TGA) was performed using a STA 6000 (Perkin Elmer), with a heating rate of 5°C min^{-1} up to 500°C and under nitrogen, calculating the amount of PP in the samples with the weight loss starting at around 350°C . Mercury Intrusion

Porosimetry measurements were made in an Autopore IV 9510 (Micromeritics). Scanning Electron Microscopy images were obtained in a Teneo (FEI, Thermo Fisher) equipped with ETD, CBS and EDS (Ametek) detection. X-Ray Diffraction patterns were collected in an automatic Diffractometer, employing a X'pert-MPD (Philips) with $\text{Cu } K_\alpha$ radiation $\lambda = 1.5406 \text{ \AA}$ at 40 kV and 40 mA ; diffractograms were refined and compared using ^oMatch software (Crystal Impact).

Electrolyte preparation

A mixed solvent strategy was employed to match the potential of the soluble molecule to the one of the LFP, so a mixture DMSO:H₂O (20:80, in vol.) was prepared and then, LiCl was added (0.5 M). For all the experiments 0.1 M $\text{K}_4\text{Fe}(\text{CN})_6$ or $\text{K}_3\text{Fe}(\text{CN})_6$ electrolytes were prepared.

Kinetics experiments

Around 300 mg of each material were mixed with 50 mL of 0.1 M $\text{K}_3\text{Fe}(\text{CN})_6$ electrolyte. Under these conditions, the oxidized mediator was in a huge stoichiometric excess (5 to 2) to avoid reaching relative concentrations of the oxidized form of the mediator smaller than 50% (if this happens, the reaction would have stopped due to the lower electrochemical potential of the solution according to Nernst equation and not due to limitations related with the solid properties). Variation in $\text{Fe}(\text{CN})_6^{3-}$ concentration was followed by UV-VIS in a spectrophotometer V-650 UV-VIS (Jasco), measuring the absorbance at $\lambda = 420 \text{ nm}$, since the spectrum of this specie present a maximum at this wavelength, while the reduced form ($\text{Fe}(\text{CN})_6^{4-}$) does not absorb.

Redox flow battery setup

Electrolyte tanks were fed with 15 mL of 0.1 M $\text{K}_4\text{Fe}(\text{CN})_6$ (1.5 mmol, 40.2 mAh, catholyte) and 50 mL 0.1 M $\text{K}_3\text{Fe}(\text{CN})_6$ (anolyte). The solutions were pumped (Pump Drive PD-5001, Heidolph) to the electrochemical cell (C-Flow 1×1, C-Tech) with a flow rate of 10 mL min^{-1} . Inside the cell, graphite felts (6.35 mm thick, 99%, Alfa Aesar) thermally activated (450°C , 30 h, air) were used as electrodes and Nafion N115 (Ion Power) as membrane. For the experiments with solid boosters, a separated tank connected to the catholyte one was placed containing 250 mg of LFP0.5sint or LFP1.0sint. The electrochemical cell was controlled by VSP3e multichannel potentiostat (Biologic Ins.) for the obtention of GCD curves obtained at different current densities (1 and 5 mA cm^{-2}).

Acknowledgements

The author Jose F. Vivo-Vilches acknowledges support from the CONEX-Plus programme funded by Universidad Carlos III de Madrid and the European Union's Horizon 2020 research and innovation programme under the Marie Skłodowska-Curie grant agreement No. 801538. The authors also thank the Agencia Española de Investigación/Fondo Europeo de Desarrollo Regional (FEDER/UE) for funding the project PID2019-106662RBC43. This work has also been supported by Comunidad de Madrid (Spain) through two projects: multiannual agreement with UC3M ("Excellencia para el Profesorado Universitario" – EPUC3M04) – Fifth regional research plan 2016–2020, and DROMADER-CM (Y2020/NMT6584).

Conflict of Interest

The authors declare no conflict of interest.

Data Availability Statement

The data that support the findings of this study are available from the corresponding author upon reasonable request.

Keywords: energy storage • powder extrusion molding • redox flow batteries • solid boosters

- [1] S. Sarwar, W. Chen, R. Waheed, *Renewable Sustainable Energy Rev.* **2017**, *76*, 9.
- [2] R. M. Elavarasan, *Eur. J. Sustain. Dev. Res.* **2018**, *3*, 1.
- [3] O. Ellabban, H. Abu-Rub, F. Blaabjerg, *Renewable Sustainable Energy Rev.* **2014**, *39*, 748.
- [4] R. B. Jackson, C. Le Quéré, R. M. Andrew, J. G. Canadell, G. P. Peters, J. Roy, L. Wu, *Environ. Res. Lett.* **2017**, *12*, 110202.
- [5] G. Chidichimo, L. Filippelli, *Int. J. Photoenergy* **2010**, *2010*, DOI 10.1155/2010/123534.
- [6] L. A. Kosyachenko, *Semiconductors* **2006**, *40*, 710.
- [7] G. E. Halkos, E. C. Gkampoura, *Energies* **2020**, *13*, 2906.
- [8] N. K. C. Nair, N. Garimella, *Energy Build.* **2010**, *42*, 2124.
- [9] A. G. Olabi, *Energy* **2017**, *136*, 1.
- [10] M. C. Argyrou, P. Christodoulides, S. A. Kalogirou, *Renewable Sustainable Energy Rev.* **2018**, *94*, 804.
- [11] M. Skyllas-Kazacos, M. H. Chakrabarti, S. A. Hajimolana, F. S. Mjalli, M. Saleem, *J. Electrochem. Soc.* **2011**, *158*, R55.
- [12] A. Parasuraman, T. M. Lim, C. Menictas, M. Skyllas-Kazacos, *Electrochim. Acta* **2013**, *101*, 27.
- [13] A. Z. Weber, M. M. Mench, J. P. Meyers, P. N. Ross, J. T. Gostick, Q. Liu, *J. Appl. Electrochem.* **2011**, *41*, 1137.
- [14] K. Lourenssen, J. Williams, F. Ahmadpour, R. Clemmer, S. Tasnim, *J. Energy Storage* **2019**, *25*, 100844.
- [15] B. Sun, M. Skyllas-Kazacos, *Electrochim. Acta* **1992**, *37*, 1253.
- [16] M. Skyllas-Kazacos, F. Grossmith, *J. Electrochem. Soc.* **1987**, *134*, 2950.
- [17] J. F. Vivo-Vilches, B. Karakashov, A. Celzard, V. Fierro, R. El Hage, N. Brosse, A. Dufour, M. Etienne, *Batteries* **2021**, *7*, 55.
- [18] B. Li, J. Liu, *Natl. Sci. Rev.* **2017**, *4*, 91.
- [19] F. Pan, Q. Wang, *Molecules* **2015**, *20*, 20499.
- [20] S. R. Narayan, A. Nirmalchandar, A. Murali, B. Yang, L. Hooper-Burkhardt, S. Krishnamoorthy, G. K. S. Prakash, *Curr. Opin. Electrochem.* **2019**, *18*, 72.
- [21] J. Luo, A. Sam, B. Hu, C. DeBruler, X. Wei, W. Wang, T. L. Liu, *Nano Energy* **2017**, *42*, 215.
- [22] T. Páez, A. Martínez-Cuezva, J. Palma, E. Ventosa, *ACS Appl. Energ. Mater.* **2019**, *2*, 8328.
- [23] Q. Huang, H. Li, M. Grätzel, Q. Wang, *Phys. Chem. Chem. Phys.* **2013**, *15*, 1793.
- [24] X. Li, *Joule* **2019**, *3*, 2066.
- [25] J. Ye, L. Xia, C. Wu, M. Ding, C. Jia, Q. Wang, *J. Phys. D* **2019**, *52*, 443001.
- [26] J. F. Vivo-Vilches, A. Nadeina, N. Rahbani, V. Seznec, D. Larcher, E. Baudrin, *J. Power Sources* **2021**, *488*, 229387.
- [27] M. Zhou, Y. Chen, M. Salla, H. Zhang, X. Wang, S. R. Mothe, Q. Wang, *Angew. Chem. Int. Ed.* **2020**, *59*, 14286.
- [28] E. Zanzola, S. Gentil, G. Gschwend, D. Reynard, E. Smirnov, C. R. Dennison, H. H. Girault, P. Peljo, *Electrochim. Acta* **2019**, *321*, 134704.
- [29] R. Yan, Q. Wang, *Adv. Mater.* **2018**, *30*, 1802406.
- [30] Q. Huang, J. Yang, C. B. Ng, C. Jia, Q. Wang, *Energy Environ. Sci.* **2016**, *9*, 917.
- [31] J. Yu, L. Fan, R. Yan, M. Zhou, Q. Wang, *ACS Energy Lett.* **2018**, *3*, 2314.
- [32] Y. G. Zhu, Y. Du, C. Jia, M. Zhou, L. Fan, X. Wang, Q. Wang, *J. Am. Chem. Soc.* **2017**, *139*, 6286.
- [33] Y. Chen, M. Zhou, Y. Xia, X. Wang, Y. Liu, Y. Yao, H. Zhang, Y. Li, S. Lu, W. Qin, X. Wu, Q. Wang, *Joule* **2019**, *3*, 2255.
- [34] E. Zanzola, C. R. Dennison, A. Battistel, P. Peljo, H. Vrubel, V. Amstutz, H. H. Girault, *Electrochim. Acta* **2017**, *235*, 664.
- [35] M. Zhou, Y. Chen, Q. Zhang, S. Xi, J. Yu, Y. Du, Y.-S. Hu, Q. Wang, *Adv. Energy Mater.* **2019**, *9*, 1901188.
- [36] R. Elango, A. Demortière, V. De Andrade, M. Morcrette, V. Seznec, *Adv. Energy Mater.* **2018**, *8*, 1703031.
- [37] C. de la Torre-Gamarra, M. E. Sotomayor, J. Y. Sanchez, B. Levenfeld, A. Várez, B. Laík, J. P. Pereira-Ramos, *J. Power Sources* **2020**, *458*, 228033.
- [38] M. E. Sotomayor, C. de la Torre-Gamarra, B. Levenfeld, J. Y. Sanchez, A. Várez, G. T. Kim, A. Varzi, S. Passerini, *J. Power Sources* **2019**, *437*, 226923.
- [39] S. D. Lacey, D. J. Kirsch, Y. Li, J. T. Morgenstern, B. C. Zarket, Y. Yao, J. Dai, L. Q. Garcia, B. Liu, T. Gao, S. Xu, S. R. Raghavan, J. W. Connell, Y. Lin, L. Hu, *Adv. Mater.* **2018**, *30*, 1705651.
- [40] A. Nadeina, P. Rozier, V. Seznec, *Energy Technol.* **2020**, *8*, 1901304.
- [41] M. E. Sotomayor, C. de La Torre-Gamarra, W. Bucheli, J. M. Amarilla, A. Várez, B. Levenfeld, J. Y. Sanchez, *J. Mater. Chem. A* **2018**, *6*, 5952.

Manuscript received: January 28, 2022

Revised manuscript received: March 28, 2022

Accepted manuscript online: March 30, 2022

Version of record online: April 21, 2022